ACS APPLIED MATERIALS & INTERFACES

www.acsami.org

Research Article

Superparamagnetic Superparticles for Magnetic Hyperthermia Therapy: Overcoming the Particle Size Limit

Supun B. Attanayake,[⊥] Minh Dang Nguyen,[⊥] Amit Chanda, Javier Alonso, Iñaki Orue, T. Randall Lee,* Hariharan Srikanth, and Manh-Huong Phan*

Cite This: *ACS Appl. Mater. Interfaces* 2025, 17, 19436−19445

Read Online

ACCESS | Metrics & More | Article Recommendations | Supporting Information

ABSTRACT: Iron oxide (e.g., Fe_3O_4 or γ-Fe_2O_3) nanoparticles are promising candidates for a variety of biomedical applications ranging from magnetic hyperthermia therapy to drug delivery and biodetection due to their superparamagnetism, nontoxicity, and biodegradability. While particles of small size (below a critical size, ∼20 nm) display superparamagnetic behavior at room temperature, these particles tend to penetrate highly sensitive areas of the body such as the blood−brain barrier, leading to undesired effects. In addition, these particles possess a high probability of retention, which can lead to genotoxicity and biochemical toxicity. Increasing particle size is a means for addressing these problems but also suppresses the superparamagnetism. We have overcome this particle size limit by synthesizing unique polycrystalline iron oxide nanoparticles composed of multiple nanocrystals of 10 to 15 nm size while tuning particle size from 160 to 400 nm. These so-called superparticles preserve superparamagnetic characteristics and exhibit excellent hyperthermia responses. The specific absorption rates exceed 250 W/g (H_{AC} = 800 Oe, f = 310 kHz) at a low concentration of 0.5 mg/mL, indicating their capability in cancer treatment with minimum dose. Our study underscores the potential of size-tunable polycrystalline iron oxide superparticles with superparamagnetic properties for advanced biomedical applications and sensing technologies.

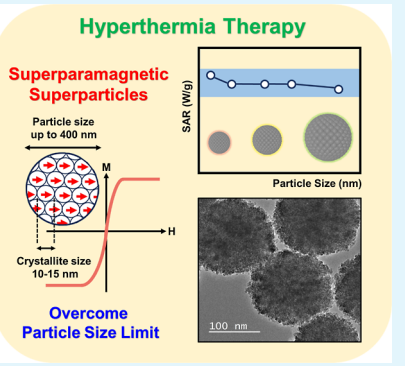

KEYWORDS: *superparticles, superparamagnetism, iron oxide nanoparticles, polycrystalline nanoparticles, magnetic hyperthermia, biomedical applications*

INTRODUCTION

Nanotechnology, the science of material manipulation at the atomic level, continues to play a significant role in everyday applications.[1−5] Its impact spans across diverse fields, including electronics, computing, medicine, healthcare, energy, and environmental sectors. Traditionally, the dimensions, shapes, and compositions of materials have been central to nanotechnology research.[6,7] However, these parameters have become secondary to the control of phase-tunability and structural ordering, which allows for the fine-tuning of nanostructures for current and future applications.[6,8−12]

Magnetic hyperthermia therapy utilizes magnetic nanoparticles (magnetite Fe_3O_4 or maghemite γ-Fe_2O_3) to generate heat through the induction of an alternating current (AC) magnetic field.[13−17] When exposed to this AC magnetic field, magnetic nanoparticles can elevate the temperature of the body from the natural level to the effective hyperthermia range of 40 to 43 °C, making them highly efficient for cancer treatment.[13,14] Hyperthermia therapy has been extensively explored as a secondary cancer treatment process with minimal adverse effects on the body while ensuring high efficacy in combating cancers via direct and indirect involvement.[13,18−21] The U.S. Food and Drug Administration has approved certain iron oxide compositions and spherical nanostructures for the usability in many treatment processes.[22−25] The large-scale usage of such therapeutic technologies, due to their less invasive nature and minimal side effects, has further given hope in making them more effective and safer.[26] The application of nanostructures in highly sensitive areas of the body such as the remarkably sensitive blood−brain barrier—a semipermeable membrane and the gateway to the central nervous system—tends to carry an imminent high risk to the life of a patient as particles in the nanolevel possess the caliber to pass through.[27−29] Therefore, it is essential to exploit magnetic nanoparticles with tunable sizes for such applications.

Unlike ferro/ferri-magnetism, superparamagnetism, which generally tends to establish in structures less than 20 nm (with zero remanent magnetization, $M_r \sim 0$ and coercivity, $H_c \sim 0$), is advantageous due to its easy manipulation, detectability, higher efficacy, and controllability and is attractive for use in hyperthermia treatment processes, drug delivery and targeting,

Received: December 29, 2024
Revised: February 24, 2025
Accepted: March 17, 2025
Published: March 20, 2025

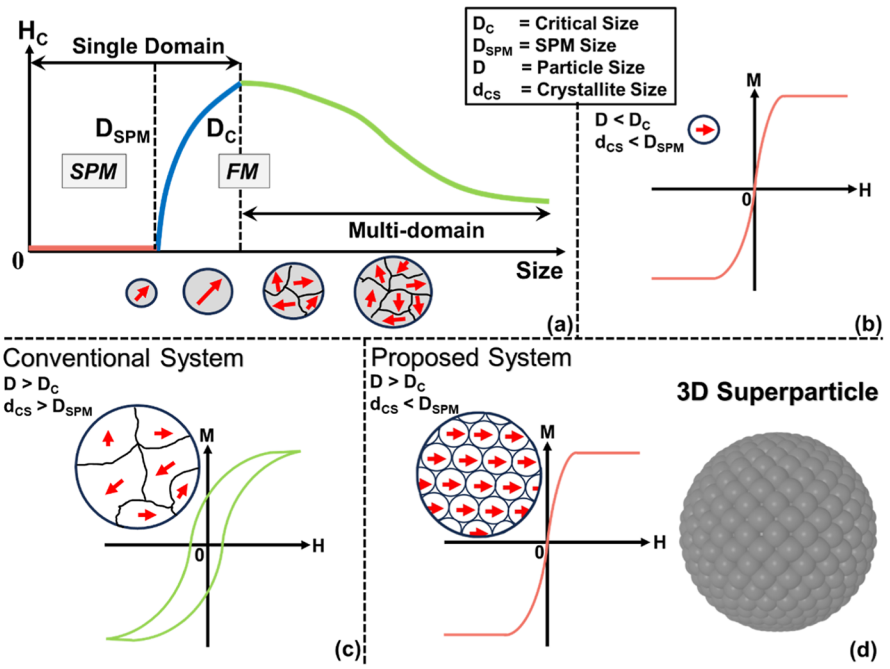

Figure 1. (a) Qualitative behavior of the coercivity and the domain boundaries in nanoparticles with size, (b) hysteresis loop of SPM particles with no coercivity ($H_c = 0$) and remanent magnetization ($M_r = 0$), (c) hysteresis loop of FM or FiM MD particles with nonzero coercivity ($H_c \neq 0$) and remanent magnetization ($M_r \neq 0$), and (d) hysteresis loop, domain states, and a 3D visualization of a SUPA showing SPM characteristics.

biodetection, and magnetic memory devices.[30−34] Traditionally, magnetic hyperthermia has primarily focused on the use of single-domain iron oxide nanoparticles with superparamagnetic (SPM) properties.[13,14,16] The use of SPM nanostructures has been further supported in hyperthermia treatments due to the facilitation of low agglomeration levels with increased dispersibility but without remanent magnetization, as the magnetization is easily flipped by the thermal energy, which exceeds the magnetic anisotropy energy.[35,36] However, due to their small size, these nanoparticles exhibit limited heating efficiency, arising from their low magnetization. Transitioning to larger nanoparticles with greater magnetization can enhance heat generation efficiency but often leads to the emergence of ferromagnetic (FM) or ferrimagnetic (FiM) properties, which gives rise to magnetic clustering due to strong magnetic dipole interactions.[11,15] As noted above, the smaller size of the nanoparticles also raises concerns about their ability to penetrate highly sensitive areas, which can give rise to potential issues related to genotoxicity and biochemical toxicity. In this context, the use of large and size-tunable polycrystalline nanoparticles with SPM properties offers an efficient solution to address the existing problems of single-domain magnetic nanoparticles.

The synergistic approach required to protect superparamagnetism while mitigating the risk in vulnerable areas has led us to scrutinize the structures more closely and propose a novel approach, as illustrated in Figure 1. Very large polycrystalline iron oxide nanoparticles, hereby named superparticles (SUPAs), in the particle size range of 150 to 400 nm, can be synthesized, ruling out potential hazards while preserving the SPM nature owing to the 10 to 15 nm sizes of nanocrystals (crystallite size/grain size) within each SUPA that are smaller than the SPM size limit (~20 nm).[37−39] In this study, our emphasis was on exploring the magnetic hyperthermia characteristics of SPM SUPAs in a medium of 2% agar since it closely replicates conditions found in biological environments.[40−42] This novel approach has shown the potential of our SUPAs for the benefit of global cancer treatment since nearly 20 million new cancer patients and 10 million deaths are reported annually due to cancer and cancer-related effects.[43] The preservation of superparamagnetism in SUPAs with a particle size tunability of up to 400 nm also highlights them as excellent candidates for many other applications, including the detection of single particle-based cells and targeted drug delivery.

NOVEL APPROACH TO OVERCOMING THE SUPERPARAMAGNETIC PARTICLE SIZE LIMIT

Magnetic nanostructures, ranging from a few nanometers to a few hundred nanometers, offer the capacity to tune their magnetic properties based on size, shape, crystallinity, and composition.[6,16,44−46] The SPM behavior observed in FM and FiM materials implies a magnetization versus magnetic field response with zero coercivity (H_c) and zero remanence magnetization (M_r) above the blocking temperature (T_B).[44] Upon size reduction, H_c varies with particle/grain size in a complex manner;[44,47] it increases with decreasing particle/grain size for MD magnetic systems (particle/grain size, $D > D_c$), reaches a maximum at a critical size (D_c) at which the system transforms from the multidomain (MD) state to the single domain (SD) state, declines to zero when particle/grain size decreases to D_{SPM} (the SPM size limit), and remains zero below D_{SPM} (Figure 1a). In the MD regime, FM or FiM materials generally possess significant H_c values since grain boundaries inhibit propagation of the magnetization reversal or magnetic domain boundary movement, which depends on the magnetic anisotropy and nucleation and growth of reverse domains.[48,49] As the structure morphs into an SD from an MD system, it becomes increasingly difficult for the resulting SD to align with the applied field, yielding the maximum H_c at the D_c. With further decreases in particle/grain size, the thermal

https://doi.org/10.1021/acsami.4c22386
ACS Appl. Mater. Interfaces 2025, 17, 19436−19445

energy becomes increasingly important in governing the spin orientation above a certain critical temperature.[50]

This mechanism enables the structures to show SPM behavior with no coercivity and no remanent magnetization (Figure 1b), as the crystallite size (d_{cs}) of the structure falls below the D_{SPM}. Unlike the cases of large SD FM or FiM particles or MD FM or FiM particles with $d_{cs} > D_{SPM}$ (Figure 1c), we propose the creation of large polycrystalline particles composed of multinanocrystals with $d_{cs} < D_{SPM}$, securing the SPM feature but with average particle size well above D_c offering impassability through vital barriers (Figure 1d). In this scenario, the average diameter of these SPM polycrystalline particles, reaching up to 400 nm, can far exceed that of the SD/MD FM or FiM particles that can span between 70 and 100 nm in diameter for magnetite, with variations based on their shape.[51,52]

RESULTS AND DISCUSSION

Structural Characterization. The structural evaluation of SUPA samples was initially carried out using scanning electron microscopy (SEM) to determine general morphology and uniformity. The sizes of the SUPA system enabled us to categorize them at varying particle sizes of up to 400 nm, as summarized in Table 1. The uniformity of the structures in all five samples was consistent with no significant morphological deviations, as shown in Figure 2a,b for samples S2 and S3, respectively. SEM images of samples S1, S4, and S5 and all size distribution histograms are presented in Figure S1. The hydrodynamic size distribution histograms for samples S1, S4, and S5 are shown in Figure S2, confirming that the SPM properties of these particles enable effective dispersion across the particle size range, making them advantageous for biomedical applications.

Table 1. Particle Size (D), Crystalline Size (d_{cs}), Saturation Magnetization (M_s), Coercivity (H_c), and Specific Absorption Rate (SAR) of the Iron Oxide Superparticles[a]

sample	D (nm)	d_{cs} (nm)	SAR (W/g)	M_s at 300 K (emu/g)	H_c at 300 K (Oe)
S1	159 ± 11	12	286	66	~0
S2	175 ± 11	15	253	68	~0
S3	234 ± 15	12	251	60	~0
S4	271 ± 31	10	252	62	~0
S5	375 ± 37	10	241	61	~0

[a]SAR values were measured in agar (0.5 mg/mL) at an AC field of 800 Oe and a frequency of 310 kHz.

Furthermore, transmission electron microscopy (TEM) was employed to evaluate the structural integrity, interparticle adjacency, and superficial crystallite distribution (Figure 2c–e). Upon closer examination through subsequent qualitative analysis, we found that the average crystallite size (d_{cs}) remained consistently below 15 nm across all the structures (see Table 1). The selected area electron diffraction (SAED) pattern, shown in the inset of Figure 2c for sample S3, exhibits clear diffraction spots confirming the crystalline nature of SUPAs,[53] which reflects the long-range order inherent in these crystalline structures. The planes can be indexed back to magnetite composition, and the presence of dislocations in the structure has led to the streaks, and the partial rings illustrate the preferred orientations in the structures.[53] A TEM image of sample S1 at a lower magnification, as shown in Figure S3, further confirms the uniformity of the nanoparticle structures. The structure and composition were further examined using X-ray diffraction (XRD). As shown in Figure 2f, all of the XRD data show well-defined peaks, revealing the good crystallinity of the SUPAs. The position and relative intensities of these peaks match well with those of magnetite structure, confirming the presence of magnetite (Fe_3O_4) as a major phase in all of the samples (Fe_3O_4 JCPDS card number: 01-088-0315). The weaker intensity of the XRD patterns and the negligible presence of minor (111) peaks in the two largest particle sizes (271 and 375 nm) can be attributed to the smaller crystallite size within the larger particle structure. This hypothesis has been further confirmed by X-ray photoelectron spectroscopy (XPS) analysis (refer to Supporting Information, Figure S4). All samples exhibited the presence of major phase magnetite (Fe_3O_4) and minor phase maghemite (γ-Fe_2O_3). This is consistent with the magnetic data obtained from the physical property measurement system (PPMS), which are presented and discussed below.

Magnetic Properties. The magnetic properties of the SUPA samples were characterized by a vibrating sample magnetometer equipped within a PPMS from Quantum Design. The temperature dependence of the magnetization, $M(T)$ with zero-field cooled (ZFC) and field-cooled (FC) curves for all samples, was measured sequentially over a 10 K $\leq T \leq$ 350 K range in the presence of a $\mu_0 H$ = 0.05 T applied field. Figure 3a shows the $M(T)$ curves of a representative sample, S1. The $M(T)$ data of the remaining samples are displayed in Figure S5. It is generally understood that FC magnetization curves tend to flatten out when reaching lower temperatures, which indicates that the sample has kept magnetization constant, while upward or downward shifting of the FC magnetization curve at low temperatures hints at interactions between particles that become more prominent as thermal energy decreases.[45] Figure 3a shows that as the thermal energy decreases, the magnetization drops since the attractions between SUPAs have made it difficult to be aligned with the applied magnetic field. Similar behavior was observed across other samples as well (refer to Supporting Information, Figure S5).

We recall that a peak or maximum observed in a ZFC $M(T)$ curve is commonly identified as the average blocking temperature (T_B) of a nanoparticle system above which H_C tends to approach zero with a minimal temperature-dependent change.[7] As observed in Figures 3a and S5, a conspicuous cusp or peak is evident in the ZFC magnetization curves at T_B^P−250 K across all SUPA samples. However, this should not be simply attributed to the average blocking temperature of SUPAs. Instead, it likely represents the onset temperature of magnetic ordering of the nanocrystals within each SUPA. The weak interactions among these nanocrystals are also expected to contribute to this cusp. This behavior has been observed regardless of particle size variations, ranging from 160 nm (S1) to 370 nm (S5), as can be seen in Figure S5. It is anticipated that all SUPA samples should manifest an SPM-like feature at $T > T_B^P$. The absence of magnetic hysteresis in the $M(H)$ loops observed for all SUPA samples has indeed confirmed the SPM behavior at room temperature (see insets of Figures 3c,d, and S6). A detailed analysis of the H_c vs T plots for all samples, as showcased in Figure 3b and its inset for sample S1 (D = 160 nm) and sample S5 (D = 370 nm), revealed a notable increase in H_c below $T_B^C \sim 150$ K, marking a clear transition from the SPM to FM or FiM (blocked) state. It is noteworthy that the

https://doi.org/10.1021/acsami.4c22386
ACS Appl. Mater. Interfaces 2025, 17, 19436−19445

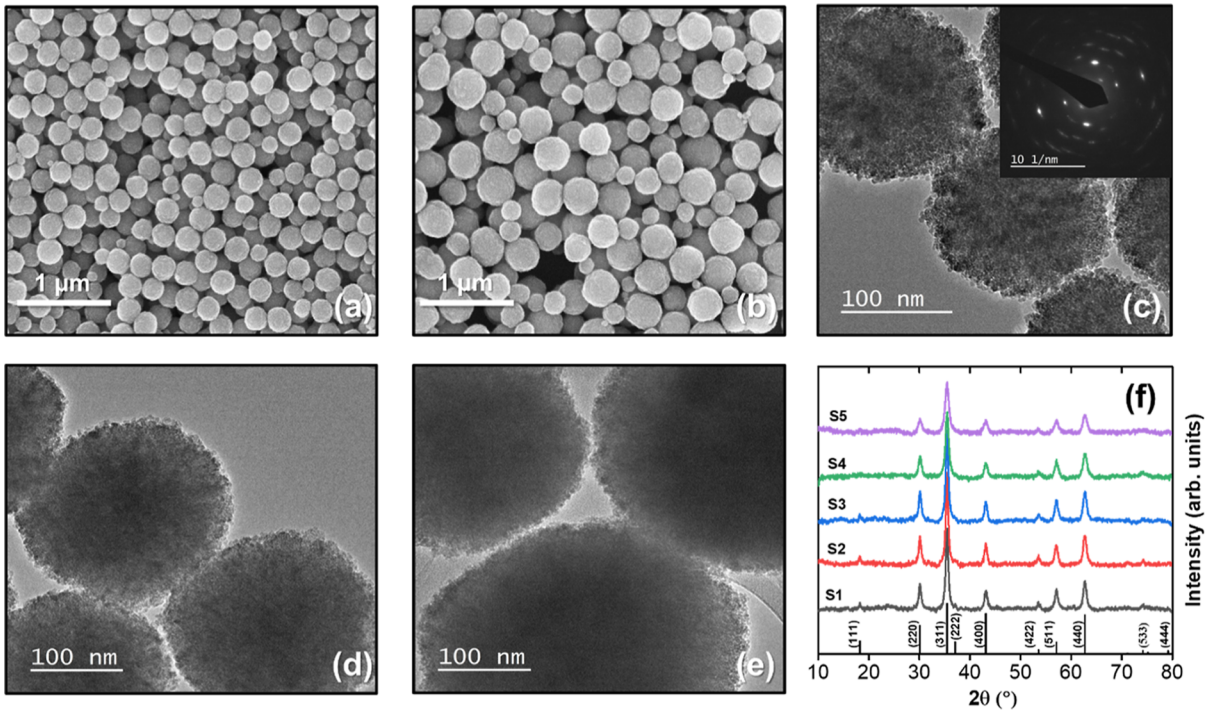

Figure 2. SEM images of samples (a) S2 and (b) S3; TEM images of samples (c) S2, (d) S3, and (e) S5. The inset of (c) shows a SAED pattern of sample S2. (f) XRD patterns for all samples. The positions of the *hkl* reflections for bulk Fe_3O_4 are marked for reference.

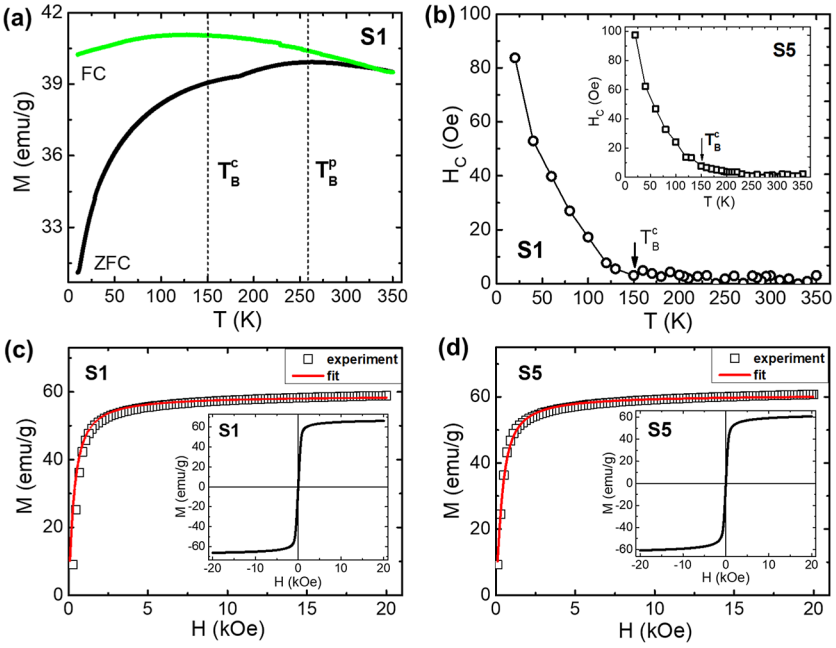

Figure 3. Magnetic characteristics of samples: (a) ZFC and FC $M(T)$ curves measured in an applied field of 0.05 T for sample S1 and (b) coercivity change with temperature for sample S1 and sample S5 (inset). Experimental and fitted M-H curves at 300 K, with the $M(H)$ loops at 300 K shown in the insets, for (c) sample S1 and (d) sample S5. The fits were conducted utilizing the SPM model (eq 1).

significant decrease in magnetization (M) below ~150 K in the ZFC $M(T)$ curve (Figure 3a) correlates with the pronounced increase in H_c as the temperature drops below this threshold (Figure 3b), suggesting the blocking of nanocrystals within each SUPA occurring below T_B^C ~150 K. Herein, T_B^C refers to the average blocking temperature of nanocrystals encapsulated within SUPAs. Our findings underscore that the magnetic properties of SUPAs are primarily determined by the size of the nanocrystals composing each SUPA. The observation of broadened ZFC $M(T)$ curves across all SUPA samples (Figures 3a and S5) is notable, likely stemming from competing interactions among nanocrystals within each SUPA and among different SUPAs, as well as from the size distributions of nanocrystals and SUPAs. Another note of interest is that the partial alignment of nanocrystals within each SUPA, as observed in the SAED pattern (inset of Figure 2c), may influence the magnetic properties of the SUPAs. However, it is difficult to draw definitive conclusions at this stage, as we

https://doi.org/10.1021/acsami.4c22386
ACS Appl. Mater. Interfaces 2025, 17, 19436−19445

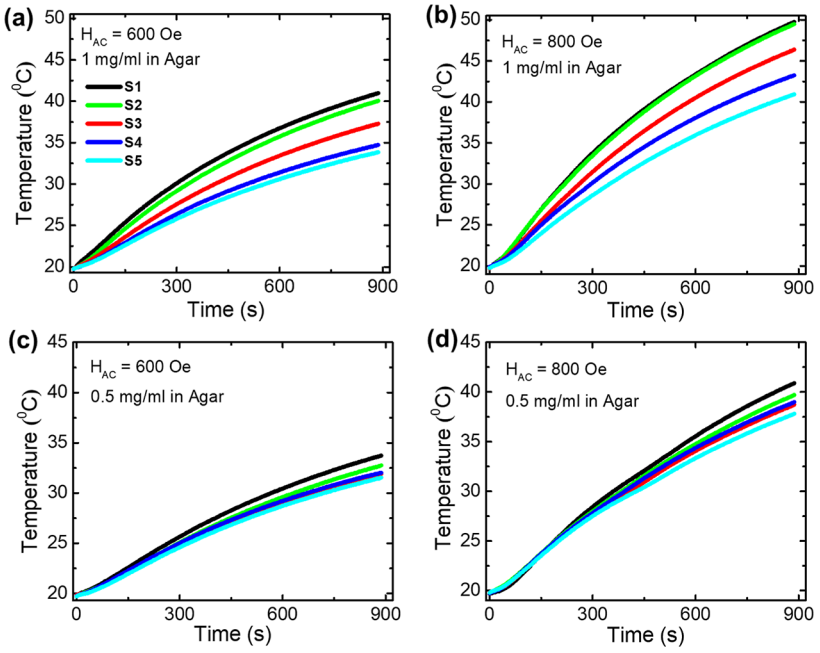

Figure 4. Temperature vs time measurements or heating curves for all five samples at concentrations of 1 and 0.5 mg/mL in the presence of (a,c) 600 Oe AC fields and (b,d) 800 Oe AC fields at a constant frequency of 310 kHz.

are unable to synthesize a randomly aligned polycrystalline structure, nor have we found relevant reports on the magnetic behavior of nanoparticles with randomly aligned primary crystals. This aspect warrants further investigation to fully understand the magnetism of the SUPA system.

To provide a deeper insight into the SPM behavior, we fitted the room temperature $M(H)$ loops for all samples using a well-known SPM model[54]

$$M(H) = \int_0^\infty M_0 L\left(\frac{\mu_0 M_S V H}{k_B T}\right) f(D) dD \quad (1)$$

where V and D are the volume and diameter of the nanocrystals, respectively; M_0 is the saturation magnetization reached in the experimental $M-H$ loops; $L(x) = \coth(x)\text{-}1/x$ is the so-called Langevin function; and M_S is the theoretical saturation magnetization of magnetite (i.e., ∼450 emu cm^{-3} for bulk magnetite at 300 K).[55] The function $f(D)$ corresponds to the particle size distribution; in our case, we have assumed a log-normal size distribution, typical for nanoparticles, as shown below

$$f(D) = \frac{1}{D\beta\sqrt{2\pi}} \cdot \exp\left(-\frac{(\ln D - \ln \alpha)^2}{2\beta^2}\right) \quad (2)$$

where α and β are fitting parameters, and the other fitting parameter is M_0. From the fittings, we can estimate the average "magnetic diameter" $\bar{D}$ and standard deviation σ of the nanoparticles

$$\bar{D} = \alpha \exp(\beta^2/2),\ \sigma^2 = \bar{D}^2\left(\frac{\bar{D}^2}{\alpha^2} - 1\right) \quad (3)$$

A good fit was obtained for all SUPA samples, as showcased in Figure 3c,d for samples S1 and S5, respectively. The fitting results for other samples are also included in the Supporting Information (Figure S7). The estimated average size and standard deviation are $\bar{D}$ = 9.4 nm and σ = 0.1 nm for S1, and $\bar{D}$ = 9.3 nm and σ = 0.9 nm for S5, respectively. These values are close to the ones obtained by TEM for the crystallites (see Table 1), confirming that at 300 K these nanocrystallites are the ones dominating the SPM-like behavior of the SUPAs. These findings are in agreement with our aforementioned interpretation of the ZFC-FC M(T) curves. It is noteworthy that through the careful control of crystallite size to remain below the SPM threshold ($d_{cs} < S_{SPM}$), we have successfully engineered SPM SUPAs, offering the capability to tune particle sizes up to 400 nm. In other words, the SPM characteristics of SUPAs are primarily influenced by the size of the nanocrystals within each individual SUPA, rather than the size of the SUPA itself. While tuning the particle size between 160 and 400 nm, consistent values of M_s were maintained across all SUPA samples (refer to Table 1). These consistent characteristics hold significant promise for diverse biomedical applications. We note further that the optimum crystallite size range for maintaining SPM properties while preserving high saturation magnetization is 10 to 15 nm. Crystallite sizes below 10 nm retain superparamagnetism but have reduced magnetization capability,[56] while sizes above 15 nm might exhibit FM behavior.[11] Additionally, the observation of Verwey transition features in the ZFC-FC $M(T)$ curves, measured in a low field of 100 Oe, along with the absence of an exchange bias effect in the $M(H)$ loops at 10 K (recorded using the ZFC and 2T-FC protocols) for samples S1, S4, and S5, as shown in Figure S8, further supports the predominance of the magnetite (Fe_3O_4) phase in the SUPA samples. This also suggests the absence of antiferromagnetic phases such as FeO and α-Fe_2O_3, which is consistent with the XRD and XPS data.

Magnetic Hyperthermia Properties. To explore the potential of SPM SUPAs for biomedical applications, we tested their magnetic hyperthermia responses. The heating efficiency of the SUPAs was evaluated in both water and 2% weight agar solution at 0.5 and 1 mg/mL, which are comparatively lower concentration levels compared to those reported previously.[57−59] The agar solution restricted the physical movement

https://doi.org/10.1021/acsami.4c22386
ACS Appl. Mater. Interfaces 2025, 17, 19436−19445

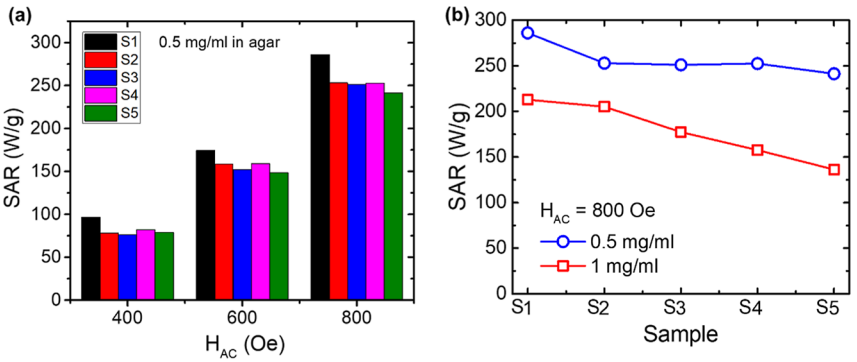

Figure 5. (a) SAR values of all SUPA samples in 2% agar at 0.5 mg/mL concentration in the presence of 400, 600, and 800 Oe AC fields and (b) SAR values of all the samples in 2% agar at concentrations of 0.5 and 1 mg/mL in an 800 Oe AC field.

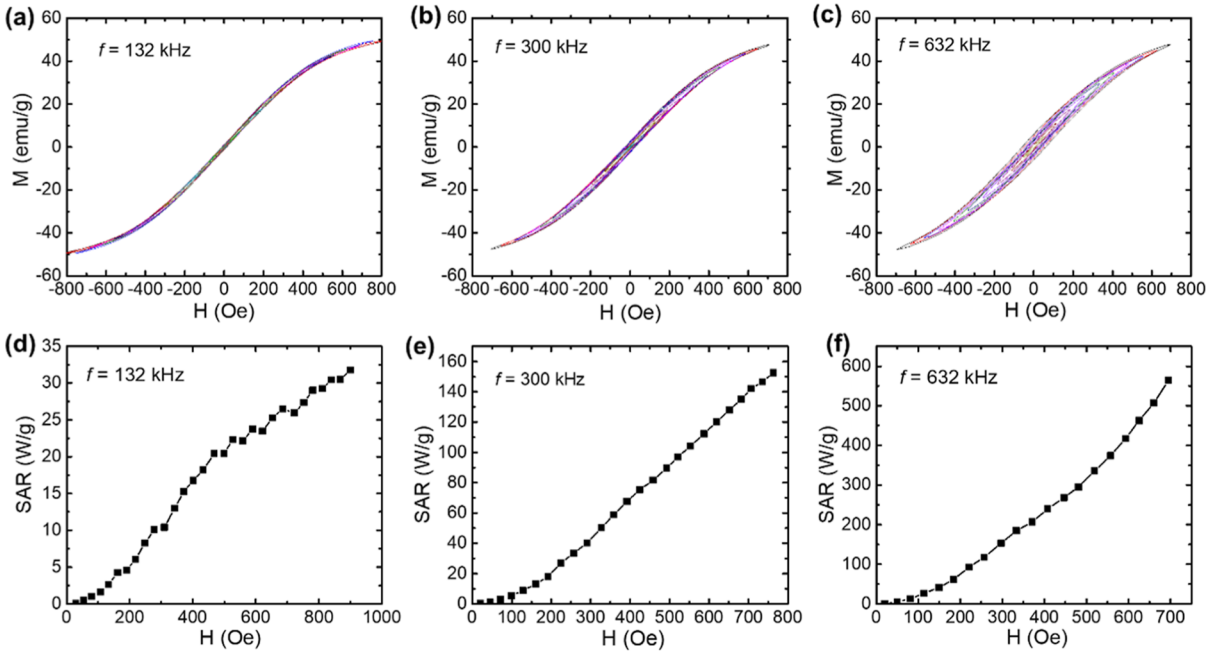

Figure 6. (a–c) Dynamic hysteresis loops measured at various frequencies and (d–f) corresponding SAR vs field curves for sample S5 at a concentration of 1.4 mg/mL.

of SUPAs, mimicking cell environments such as cell cytoplasm and extracellular matrix.[60,61] Figure 4 displays the heating curves for all samples at concentrations of 1 and 0.5 mg/mL, subjected to AC fields of 600 and 800 Oe at a constant frequency of 310 kHz. The data show that all the samples yielded consistent results, with sample S1 showing significantly higher heating capability across all concentrations. Notably, the heating capabilities of the samples for the hyperthermia treatment process were evaluated for a maximum of 15 min (900 s), which is lower than the typical treatment duration of 30 min to 1 h.[62,63]

To quantify the heating efficiency of the samples, the SAR, which is a measure of the absorption energy, usually determined from the initial rate of temperature rise, was evaluated.[64] In our computations utilizing eq 4, we derived the SAR values from the heating curves after a 60 s interval, as the SUPAs tend to stabilize over time

$$\mathrm{SAR} = \frac{\Delta T}{\Delta t} \times \frac{\mathrm{Cp}}{\varphi} \tag{4}$$

where $\Delta T/\Delta t$ represents the change in temperature with time and C_P represents the heat capacity of the liquid solvent (in this case, water with 4.186 J/g K). The symbol φ represents a unitless quantity: mass of magnetic material per unit mass of liquid solvent.

Figure 5a shows the SAR values for all the samples at 0.5 mg/mL concentration in 2% agar of which the H_{AC} of 800 Oe showed the highest SAR values, with S1 at 286 W/g obtained using initial slope/time-rise protocol assuming a minimal to no heat gain/loss.[65] The SUPAs were initially evaluated with deionized water (refer to Supporting Information, Figure S9) which led to temperature drops with the H_{AC}. These drops could be related to the movement or rearrangement of the SUPAs upon application of the AC field in water. Due to inconsistencies with the temperature drops, the heating responses of SUPAs in water were not considered for the SAR calculations. Similar to the peculiar observation related to water, the concentration increments that usually led to higher SAR values were not observed in SUPAs but rather a drop, which might be due to intensified interparticle interactions with the increased presence of SUPAs per unit volume, as

https://doi.org/10.1021/acsami.4c22386
ACS Appl. Mater. Interfaces 2025, 17, 19436−19445

shown in Figure 5b. Moreover, we conducted comprehensive field-dependent and concentration-dependent measurements, which served to deepen our aforementioned observations (refer to Supporting Information, Figure S10).

Given the similarity in the SPM properties of the SUPAs across the size range—primarily driven by their similar crystallite size—we have observed comparable M_s values (Table 1), resulting in similar SAR values (Figure 5a) when low-concentration (0.5 mg/mL) SUPAs were dispersed in agar. This is a unique and desirable characteristic of our SPM SUPAs for biomedical applications including hyperthermia therapy. However, SAR tended to decrease with increasing particle size when higher concentrations of SUPAs (e.g., 1 mg/mL) were dispersed in agar (Figure 5b) or water (Figure S9b). This suggests that smaller SUPAs exhibit more efficient heating, likely due to reduced interparticle interactions among smaller particles at higher concentrations (1 mg/mL) used for magnetic hyperthermia therapy. The effect becomes more pronounced at higher AC fields (Figures 5b and S9b). It is a combination of the large M_s and the smallest particle size (Table 1) that resulted in the largest SAR value for sample S1 (Figure 5a,b) in comparison to other samples. Furthermore, we anticipate that surface functionalization of SUPAs with a biocompatible polymer or the formation of core/shell nanoparticles such as Fe_3O_4/SiO_2 SUPAs could enhance the colloidal stability by increasing the presence of hydrophilic functional groups and reducing interparticle interactions under high AC field conditions.

To validate the SAR values mentioned above, we employed an independent method. This approach enabled us to directly measure the AC magnetic hysteresis loops and calculate the SAR values based on the area (A) enclosed by these loops, according to the following equation[66]

$$\mathrm{SAR}\left(\frac{W}{g}\right) = \frac{f}{c}\cdot A = \frac{f}{c}\cdot \oint \mu_0 M_t \, dH_t \tag{5}$$

with M_t being the instantaneous magnetization at time t, H_t being the sinusoidal magnetic field of frequency f at time t, and c being the magnetite weight concentration in the dispersing medium. The integration was conducted over a period of the oscillating magnetic field, $T = 2\pi/f$. AC magnetic hysteresis measurements were performed at various frequencies (f = 132, 300, and 638 kHz) on sample S5 possessing the largest average particle size of ~370 nm. The results obtained are displayed in Figure 6. As illustrated, narrow minor loops were consistently obtained at low AC fields across all applied frequencies (Figure 6a−c). However, with increasing AC field strength, both the area of the AC loops (Figure 6a−c) and the corresponding SAR values (Figure 6d−f) gradually increased. Notably, at 300 kHz and 800 Oe, a SAR value of approximately 150 W/g was achieved, aligning closely with the value previously estimated from calorimetric measurements (Figure 5b).[67] It is also noteworthy from Figure 6f that the SAR reached ~600 W/g as the frequency rose to 632 kHz, indicating the potential of SUPAs for magnetic hyperthermia therapy.

Finally, we compared the SAR values for our SUPAs with those obtained from other nanostructures (spheres, cubes, and rods), highlighting their superior SPM characteristics and lower concentration requirements (refer to Supporting Information, Table S1). This comparison underscores the absence of SPM behavior in typical nanostructures as particle size increases. Notably, conventionally synthesized iron oxide nanoparticles with average sizes of 40 nm or larger exhibit FiM behavior, contrasting with our SUPAs, which maintain SPM characteristics despite sizes up to 400 nm. It is also noteworthy that only half the concentration of SUPAs (0.5 mg/mL vs 1 mg/mL) is required for magnetic hyperthermia treatment compared to other candidates (Table S1). The combination of SPM properties, large and adjustable SARs, and reduced concentration requirements positions these iron oxide SUPAs as compelling contenders for a wide range of biomedical applications. For example, SUPAs can serve as heating agents or heat mediators in the core to regulate thermoresponsive shell materials for controlled drug release.

CONCLUSIONS

Polycrystalline iron oxide SUPAs with particle sizes of up to 400 nm, featuring crystallite sizes of 10−15 nm, exhibit SPM features at room temperature. We have demonstrated that if crystallite sizes are alike and below the SPM size threshold, SUPAs display SPM behavior at room temperature and enter an FM or FiM (blocked) state at a comparable temperature. Across all samples, a low concentration of 0.5 mg/mL consistently yielded a SAR exceeding 250 W/g in an 800 Oe AC field. The exceptional stability of SPM SUPAs in a 2% by-weight agar solution, at both 0.5 and 1 mg/mL concentrations, underscores their potential for in vivo studies. However, further evaluations of the cytotoxicity and biocompatibility of these SUPAs are needed, even though the composition and structures conform to internationally accredited safety agencies such as the U.S. Food and Drug Administration. The promising performance of these SPM SUPAs warrants further exploration to deepen our understanding of the underlying physics behind their mechanisms.

EXPERIMENTAL METHODS

Materials. The chemicals used for synthesis of polycrystalline SPM nanoparticles were iron(III) chloride hexahydrate (97%, Alfa Aesar), ethylene glycol (99%, Sigma-Aldrich), diethylene glycol (99%, ACROS Organics), sodium acetate anhydrous (99%, ACROS Organics), sodium acetate trihydrate (99%, Fisher), sodium acrylate (97%, Sigma-Aldrich), and polyethylene glycol (400) (Olin Mathieson Chemical Corporation). A 65 mL volume pressure vessel was purchased from Chem Glass. In addition, common solvents such as deionized water with a resistance of 18 MΩ cm (Academic Milli-Q Water System, Millipore Corporation), ethanol (200 proof, Decon Laboratories), and acetone (99%, Oakwood) were used.

Synthesis of Iron Oxide Superparticles. The polycrystalline SPM nanoparticles were synthesized by solvothermal methods in a binary solvent system containing ethylene glycol and diethylene glycol, with modifications in the technical setup and the uses of chemical additives.[11,56,68] In this method, the use of anhydrous sodium acetate (2.17 or 3.6 g) in the synthesis was found to be effective in maintaining the small crystallite size (the size of the primary crystal) at the range from 10 to 15 nm while allowing for the fabrication of large particles with diameters larger than 160 nm.[69] Initially, a pressure vessel was charged with 1.35 g of $FeCl_3{\cdot}6H_2O$ and 20 mL of the binary solvent mixture (see below). After complete dissolution of the iron chloride, an additional 20 mL of the binary solvent was added to anhydrous sodium acetate. The binary solvent system used for the synthesis consisted of 15/25 or 20/20 mL of ethylene glycol/diethylene glycol. The mixture was stirred for 30 min to ensure complete dissolution, followed by the addition of 1.2 mL of PEG (400) surfactant. The Teflon cap was securely fastened, and the pressure vessel was heated to 188 °C for refluxing over 5 h. A safety shield was used to cover the synthesis setup. After synthesis, the product was cooled to room temperature and washed with ethanol combined with magnetic separation for at least 3 cycles. It is

https://doi.org/10.1021/acsami.4c22386
ACS Appl. Mater. Interfaces 2025, 17, 19436−19445

important to note that technical parameters such as the stirring speed or slower heating rate can be used to alter the size of nanoparticles. Particularly, a faster stirring speed or a slower ramping rate can increase the average size of nanoparticles. By carefully adjusting the stirring speed and heating rate, we can optimize the synthesis method for SUPAs with a size of 235 nm to achieve smaller sizes of 159 and 175 nm. By adjusting the technical parameters, varying the solvent composition, and utilizing different amounts of sodium acetate additives, the size of polycrystalline iron oxide nanoparticles can be tuned from 160 to 400 nm.[69]

Characterizations. SEM FEI Dual Beam 235 Focused Ion Beam at an operating voltage 15 kV was used for imaging the nanoparticles. Samples were dissolved in ethanol and drop-cast onto a clean silicon wafer. TEM JEOL JEM-2010 was used with an accelerating voltage of 200 kV. Samples were prepared on TEM grids with 300-mesh holey carbon-coated copper grids (TED Pella). XRD data (SmartLab, Rigaku) were collected using Cu Kα irradiation operated at 40 kV and 44 mA with a 0.01° step size for all samples. The crystallite size was calculated by the Scherrer formula from the diffracted peak of the (311) plane at a 2θ of 35.5°. XPS analysis was conducted on a dried sample drop-cast onto a silicon wafer using a PHI 5700 X-ray photoelectron spectrometer with monochromatic Al Kα X-rays. Calibration was performed using the C 1s peak at 284.8 eV. The hydrodynamic size of the nanoparticles was determined by dynamic light scattering using a Malvern Zetasizer ZEN3600.

The magnetic measurements were performed using a PPMS by Quantum Design, Inc., utilizing the vibrating sample magnetometer option between 10 and 350 K at a maximum applied magnetic field of 2 T. Calorimetric magnetic hyperthermia experiments were carried out using 4.2 kW Ambrell Easyheat Li3542 equipment with varying AC magnetic fields (0−800 Oe) at a constant 310 kHz frequency starting at 20 °C for 900 s with 0.5 and 1 mg/mL nanoparticles in a 2% by weight agar solution prepared with deionized water. AC magnetometry measurements were carried out using a homemade setup to record the AC hysteresis loops.[70] The AC magnetic field amplitude was tuned between 0 and 80 mT, and 3 different frequencies were employed, 149 kHz, 300, and 638 kHz. Samples were again prepared in a 2% agar solution.

■ ASSOCIATED CONTENT

Supporting Information

The Supporting Information is available free of charge at https://pubs.acs.org/doi/10.1021/acsami.4c22386.

SEM images of SUPAs and size distribution; hydrodynamic size characterized by dynamic light scatterings; TEM image of sample S1; XPS spectra of SUPAs; $M(T)$ curves under ZFC and FC protocols of SUPAs at 500 Oe; $M(H)$ curves of SUPAs at 300 K; $M(H)$ results obtained from the experiment and fitting of the Langevin function; $M(T)$ at low field of 100 Oe and $M(H)$ at 10 K using ZFC and 2T-FC protocols; and heating curves at concentrations of 1 mg/mL and SAR values at 800 Oe AC field and a frequency of 310 kHz in both water and agar (PDF)

■ AUTHOR INFORMATION

Corresponding Authors

T. Randall Lee − *Department of Chemistry and the Texas Center for Superconductivity, University of Houston, Houston, Texas 77204-5003, United States;* orcid.org/0000-0001-9584-8861; Email: trlee@uh.edu

Manh-Huong Phan − *Department of Physics, University of South Florida, Tampa, Florida 33620, United States;* orcid.org/0000-0002-6270-8990; Email: phanm@usf.edu

Authors

Supun B. Attanayake − *Department of Physics, University of South Florida, Tampa, Florida 33620, United States;* orcid.org/0000-0003-0799-7889

Minh Dang Nguyen − *Department of Chemistry and the Texas Center for Superconductivity, University of Houston, Houston, Texas 77204-5003, United States*

Amit Chanda − *Department of Physics, University of South Florida, Tampa, Florida 33620, United States;* orcid.org/0000-0001-9681-0312

Javier Alonso − *Department of CITIMAC, Universidad de Cantabria, Santander 39005, Spain*

Iñaki Orue − *SGIker Medidas Magnéticas, Universidad Del País Vasco, Leioa 48940, Spain;* orcid.org/0000-0002-7496-2566

Hariharan Srikanth − *Department of Physics, University of South Florida, Tampa, Florida 33620, United States;* orcid.org/0000-0002-2541-7000

Complete contact information is available at: https://pubs.acs.org/10.1021/acsami.4c22386

Author Contributions

⊥S.B.A. and M.D.N. made equal contributions to the work.

Notes

The authors declare no competing financial interest.

■ ACKNOWLEDGMENTS

Work at USF was supported by the US Department of Energy, Office of Basic Energy Sciences, Division of Materials Science and Engineering under grant no. DE-FG02-07ER46438. J.A. acknowledges financial support from Spanish MCIN/AEI under Project PID2020-115704RB-C3., T.R. Lee thanks financial support for the research at UH from the Air Force Office of Scientific Research (AFOSR FA9550-23-1-0581; 23RT0567) and the Robert A. Welch Foundation grant nos. E-1320 and V-E-0001. H.S. acknowledges support from US National Science Foundation through grant no. NSF DMR-2327667 and also support from Alexander von Humboldt foundation for a Humboldt Research Award. M.H. Phan acknowledges the Programa de Profesores Visitantes 2023-2024 offered by the Vice-Rector of Research and Knowledge Transfer at the University of Cantabria, Spain, for supporting his visiting professorship.

■ REFERENCES

(1) Chauhan, I.; Yasir, M.; Verma, M.; Singh, A. P. Nanostructured Lipid Carriers: A Groundbreaking Approach for Transdermal Drug Delivery. *Adv. Pharm. Bull.* **2020**, *10*, 150−165.

(2) Conde, J.; Langer, R.; Rueff, J. mRNA Therapy at the Convergence of Genetics and Nanomedicine. *Nat. Nanotechnol.* **2023**, *18*, 537−540.

(3) Janjua, T. I.; Cao, Y.; Ahmed-Cox, A.; Raza, A.; Moniruzzaman, M.; Akhter, D. T.; Fletcher, N. L.; Kavallaris, M.; Thurecht, K. J.; Popat, A. Efficient Delivery of Temozolomide Using Ultrasmall Large-Pore Silica Nanoparticles for Glioblastoma. *J. Controlled Release* **2023**, *357*, 161−174.

(4) Omidiyan, M.; Srinoi, P.; Tajalli, P.; Lee, T. R. Review of Light-Activated Antimicrobial Nanoparticle−Polymer Composites for Biomedical Devices. *ACS Appl. Nano Mater.* **2024**, *7*, 8377−8391.

(5) Medhi, R.; Srinoi, P.; Ngo, N.; Tran, H.-V.; Lee, T. R. Nanoparticle-Based Strategies to Combat COVID-19. *ACS Appl. Nano Mater.* **2020**, *3*, 8557−8580.

(6) Nguyen, M. D.; Tran, H.-V.; Xu, S.; Lee, T. R. Fe_3O_4 Nanoparticles: Structures, Synthesis, Magnetic Properties, Surface

Functionalization, and Emerging Applications. *Appl. Sci.* **2021**, *11*, 11301.
(7) Kolhatkar, A. G.; Jamison, A. C.; Litvinov, D.; Willson, R. C.; Lee, T. R. Tuning the Magnetic Properties of Nanoparticles. *Int. J. Mol. Sci.* **2013**, *14*, 15977−16009.
(8) Attanayake, S. B.; Chanda, A.; Hulse, T.; Das, R.; Phan, M.-H.; Srikanth, H. Competing Magnetic Interactions and Field-Induced Metamagnetic Transition in Highly Crystalline Phase-Tunable Iron Oxide Nanorods. *Nanomaterials* **2023**, *13*, 1340.
(9) Chen, L.; Luque, R.; Li, Y. Controllable Design of Tunable Nanostructures inside Metal−Organic Frameworks. *Chem. Soc. Rev.* **2017**, *46*, 4614−4630.
(10) Jung, F. A.; Schart, M.; Bührend, L.; Meidinger, E.; Kang, J.-J.; Niebuur, B.-J.; Ariaee, S.; Molodenskiy, D. S.; Posselt, D.; Amenitsch, H.; Tsitsilianis, C.; Papadakis, C. M. Highly Tunable Nanostructures in a Doubly pH-Responsive Pentablock Terpolymer in Solution and in Thin Films. *Adv. Funct. Mater.* **2021**, *31*, 2102905.
(11) Chen, Y.-T.; Medhi, R.; Nekrashevich, I.; Litvinov, D.; Xu, S.; Lee, T. R. Specific Detection of Proteins Using Exceptionally Responsive Magnetic Particles. *Anal. Chem.* **2018**, *90*, 6749−6756.
(12) Kolhatkar, A. G.; Chen, Y.-T.; Chinwangso, P.; Nekrashevich, I.; Dannangoda, G. C.; Singh, A.; Jamison, A. C.; Zenasni, O.; Rusakova, I. A.; Martirosyan, K. S.; Litvinov, D.; Xu, S.; Willson, R. C.; Lee, T. R. Magnetic Sensing Potential of Fe_3O_4 Nanocubes Exceeds That of Fe_3O_4 Nanospheres. *ACS Omega* **2017**, *2*, 8010−8019.
(13) PéRigo, E. A.; Hemery, G.; Sandre, O.; Ortega, D.; Garaio, E.; Plazaola, F.; Teran, F. J. Fundamentals and Advances in Magnetic Hyperthermia. *Appl. Phys. Rev.* **2015**, *2*, 041302.
(14) Liu, X.; Zhang, Y.; Wang, Y.; Zhu, W.; Li, G.; Ma, X.; Zhang, Y.; Chen, S.; Tiwari, S.; Shi, K.; Zhang, S.; Fan, H. M.; Zhao, Y. X.; Liang, X.-J. Comprehensive Understanding of Magnetic Hyperthermia for Improving Antitumor Therapeutic Efficacy. *Theranostics* **2020**, *10*, 3793−3815.
(15) Chang, D.; Lim, M.; Goos, J. A. C. M.; Qiao, R.; Ng, Y. Y.; Mansfeld, F. M.; Jackson, M.; Davis, T. P.; Kavallaris, M. Biologically Targeted Magnetic Hyperthermia: Potential and Limitations. *Front. Pharmacol* **2018**, *9*, 1−20.
(16) Lavorato, G. C.; Das, R.; Alonso Masa, J.; Phan, M.-H.; Srikanth, H. Hybrid Magnetic Nanoparticles as Efficient Nanoheaters in Biomedical Applications. *Nanoscale Adv.* **2021**, *3*, 867−888.
(17) Gavilán, H.; Avugadda, S. K.; Fernández-Cabada, T.; Soni, N.; Cassani, M.; Mai, B. T.; Chantrell, R.; Pellegrino, T. Magnetic Nanoparticles and Clusters for Magnetic Hyperthermia: Optimizing Their Heat Performance and Developing Combinatorial Therapies to Tackle Cancer. *Chem. Soc. Rev.* **2021**, *50*, 11614−11667.
(18) Yi, G. Y.; Kim, M. J.; Kim, H. I.; Park, J.; Baek, S. H. Hyperthermia Treatment as a Promising Anti-Cancer Strategy: Therapeutic Targets, Perspective Mechanisms and Synergistic Combinations in Experimental Approaches. *Antioxidants* **2022**, *11*, 625.
(19) Ijff, M.; Crezee, J.; Oei, A. L.; Stalpers, L. J. A.; Westerveld, H. The Role of Hyperthermia in the Treatment of Locally Advanced Cervical Cancer: A Comprehensive Review. *Int. J. Gynecol. Cancer* **2022**, *32*, 288.
(20) Ademaj, A.; Veltsista, D. P.; Ghadjar, P.; Marder, D.; Oberacker, E.; Ott, O. J.; Wust, P.; Puric, E.; Hälg, R. A.; Rogers, S.; Bodis, S.; Fietkau, R.; Crezee, H.; Riesterer, O. Clinical Evidence for Thermometric Parameters to Guide Hyperthermia Treatment. *Cancers* **2022**, *14*, 625.
(21) Mantso, T.; Vasileiadis, S.; Anestopoulos, I.; Voulgaridou, G. P.; Lampri, E.; Botaitis, S.; Kontomanolis, E. N.; Simopoulos, C.; Goussetis, G.; Franco, R.; Chlichlia, K.; Pappa, A.; Panayiotidis, M. I. Hyperthermia Induces Therapeutic Effectiveness and Potentiates Adjuvant Therapy with Non-Targeted and Targeted Drugs in an in Vitro Model of Human Malignant Melanoma. *Sci. Rep.* **2018**, *8*, 10724.
(22) Soetaert, F.; Korangath, P.; Serantes, D.; Fiering, S.; Ivkov, R. Cancer Therapy with Iron Oxide Nanoparticles: Agents of Thermal and Immune Therapies. *Adv. Drug Delivery Rev.* **2020**, *163*−*164*, 65−83.
(23) Thakor, A. S.; Jokerst, J. V.; Ghanouni, P.; Campbell, J. L.; Mittra, E.; Gambhir, S. S. Clinically Approved Nanoparticle Imaging Agents. *J. Nucl. Med.* **2016**, *57*, 1833−1837.
(24) Bobo, D.; Robinson, K. J.; Islam, J.; Thurecht, K. J.; Corrie, S. R. Nanoparticle-Based Medicines: A Review of FDA-Approved Materials and Clinical Trials to Date. *Pharm. Res.* **2016**, *33*, 2373−2387.
(25) Revia, R. A.; Zhang, M. Magnetite Nanoparticles for Cancer Diagnosis, Treatment, and Treatment Monitoring: Recent Advances. *Mater. Today* **2016**, *19*, 157−168.
(26) Peeters, H.; van Zwol, E. M.; Brancato, L. M. C.; M C da Cunha, M. G.; Bogers, J. Systematic Review of the Registered Clinical Trials for Oncological Hyperthermia Treatment. *Int. J. Hyperthermia* **2022**, *39*, 806−812.
(27) Sutton, C. H.; Carroll, F. B. Effects of Microwave-Induced Hyperthermia on the Blood-Brain Barrier of the Rat. *Radio Sci.* **1979**, *14*, 329−334.
(28) Segarra, M.; Aburto, M. R.; Acker-Palmer, A. Blood−Brain Barrier Dynamics to Maintain Brain Homeostasis. *Trends Neurosci.* **2021**, *44*, 393−405.
(29) Shivers, R. R.; Wijsman, J. A. Chapter 19 Blood-brain barrier permeability during hyperthermia. In *Progress in Brain Research*; Sharma, H. S., Westman, J., Eds.; Elsevier, 1998; Vol. *115*, pp 413−424.
(30) Mok, H.; Zhang, M. Superparamagnetic Iron Oxide Nanoparticle-Based Delivery Systems for Biotherapeutics. *Expert Opin. Drug Delivery* **2013**, *10*, 73−87.
(31) Caizer, I. S.; Caizer, C. Superparamagnetic Hyperthermia Study with Cobalt Ferrite Nanoparticles Covered with γ-Cyclodextrins by Computer Simulation for Application in Alternative Cancer Therapy. *Int. J. Mol. Sci.* **2022**, *23*, 4350.
(32) Koplovitz, G.; Leitus, G.; Ghosh, S.; Bloom, B. P.; Yochelis, S.; Rotem, D.; Vischio, F.; Striccoli, M.; Fanizza, E.; Naaman, R.; Waldeck, D. H.; Porath, D.; Paltiel, Y. Single Domain 10 Nm Ferromagnetism Imprinted on Superparamagnetic Nanoparticles Using Chiral Molecules. *Small* **2019**, *15*, 1804557.
(33) Vodenicarevic, D.; Locatelli, N.; Mizrahi, A.; Friedman, J. S.; Vincent, A. F.; Romera, M.; Fukushima, A.; Yakushiji, K.; Kubota, H.; Yuasa, S.; Tiwari, S.; Grollier, J.; Querlioz, D. Low-Energy Truly Random Number Generation with Superparamagnetic Tunnel Junctions for Unconventional Computing. *Phys. Rev. Appl.* **2017**, *8*, 054045.
(34) Neuberger, T.; Schöpf, B.; Hofmann, H.; Hofmann, M.; von Rechenberg, B. Superparamagnetic Nanoparticles for Biomedical Applications: Possibilities and Limitations of a New Drug Delivery System. *J. Magn. Magn. Mater.* **2005**, *293*, 483−496.
(35) Suter, M.; Ergeneman, O.; Zürcher, J.; Schmid, S.; Camenzind, A.; Nelson, B. J.; Hierold, C. Superparamagnetic Photocurable Nanocomposite for the Fabrication of Microcantilevers. *J. Manuf. Syst.* **2011**, *21*, 025023.
(36) Müller, R.; Hergt, R.; Dutz, S.; Zeisberger, M.; Gawalek, W. Nanocrystalline Iron Oxide and Ba Ferrite Particles in the Superparamagnetism−Ferromagnetism Transition Range with Ferrofluid Applications. *J. Phys.: Condens. Matter* **2006**, *18*, S2527.
(37) Wang, T.; LaMontagne, D.; Lynch, J.; Zhuang, J.; Cao, Y. C. Colloidal Superparticles from Nanoparticle Assembly. *Chem. Soc. Rev.* **2013**, *42*, 2804−2823.
(38) Thapa, R. K.; Kim, J. O. Nanomedicine-Based Commercial Formulations: Current Developments and Future Prospects. *J. Pharm. Investig.* **2023**, *53*, 19−33.
(39) Rodríguez, F.; Caruana, P.; De la Fuente, N.; Español, P.; Gámez, M.; Balart, J.; Llurba, E.; Rovira, R.; Ruiz, R.; Martín-Lorente, C.; Corchero, J. L.; Céspedes, M. V. Nano-Based Approved Pharmaceuticals for Cancer Treatment: Present and Future Challenges. *Biomolecules* **2022**, *12*, 784.
(40) Alonso, J.; Khurshid, H.; Sankar, V.; Nemati, Z.; Phan, M. H.; Garayo, E.; García, J. A.; Srikanth, H. FeCo Nanowires with Enhanced

Heating Powers and Controllable Dimensions for Magnetic Hyperthermia. *J. Appl. Phys.* **2015**, *117*, 17D113.
(41) Lahiri, B. B.; Ranoo, S.; Philip, J. Effect of Orientational Ordering of Magnetic Nanoemulsions Immobilized in Agar Gel on Magnetic Hyperthermia. *J. Magn. Magn. Mater.* **2018**, *451*, 254−268.
(42) Salloum, M.; Ma, R. H.; Weeks, D.; Zhu, L. Controlling Nanoparticle Delivery in Magnetic Nanoparticle Hyperthermia for Cancer Treatment: Experimental Study in Agarose Gel. *Int. J. Hyperthermia* **2008**, *24*, 337−345.
(43) Cancer (IARC), T. I. A. for R. on. *Global Cancer Observatory*. https://gco.iarc.fr/(accessed May 15, 2024).
(44) Jun, Y.; Seo, J.; Cheon, J. Nanoscaling Laws of Magnetic Nanoparticles and Their Applicabilities in Biomedical Sciences. *Acc. Chem. Res.* **2008**, *41*, 179−189.
(45) Phan, M.-H.; Alonso, J.; Khurshid, H.; Lampen-Kelley, P.; Chandra, S.; Stojak Repa, K.; Nemati, Z.; Das, R.; Iglesias, O. ∴; Srikanth, H. Exchange Bias Effects in Iron Oxide-Based Nanoparticle Systems. *Nanomaterials* **2016**, *6*, 221.
(46) Shingte, S. D.; Phakatkar, A. H.; McKiernan, E.; Nigoghossian, K.; Ferguson, S.; Shahbazian-Yassar, R.; Brougham, D. F. Correlating Magnetic Hyperthermia and Magnetic Resonance Imaging Contrast Performance of Cubic Iron Oxide Nanoparticles with Crystal Structural Integrity. *Chem. Mater.* **2022**, *34*, 10801−10810.
(47) Herzer, G. Grain Size Dependence of Coercivity and Permeability in Nanocrystalline Ferromagnets. *IEEE Trans. Magn.* **1990**, *26*, 1397−1402.
(48) Stoner, E. C.; Wohlfarth, E. P. Interpretation of High Coercivity in Ferromagnetic Materials. *Nature* **1947**, *160*, 650−651.
(49) Livingston, J. D. A Review of Coercivity Mechanisms (Invited). *J. Appl. Phys.* **1981**, *52*, 2544−2548.
(50) Petracic, O. Superparamagnetic Nanoparticle Ensembles. *Superlattices Microstruct.* **2010**, *47*, 569−578.
(51) Reichel, V.; Kovács, A.; Kumari, M.; Bereczk-Tompa, E. ∴; Schneck, E.; Diehle, P.; Pósfai, M.; Hirt, A. M.; Duchamp, M.; Dunin-Borkowski, R. E.; Faivre, D. Single Crystalline Superstructured Stable Single Domain Magnetite Nanoparticles. *Sci. Rep.* **2017**, *7*, 45484.
(52) Li, Q.; Kartikowati, C. W.; Horie, S.; Ogi, T.; Iwaki, T.; Okuyama, K. Correlation between Particle Size/Domain Structure and Magnetic Properties of Highly Crystalline Fe_3O_4 Nanoparticles. *Sci. Rep.* **2017**, *7*, 9894.
(53) Suvorova, E. I.; Buffat, P. A. Electron Diffraction from Micro- and Nanoparticles of Hydroxyapatite. *J. Microsc.* **1999**, *196*, 46−58.
(54) Knobel, M.; Nunes, W. C.; Socolovsky, L. M.; De Biasi, E.; Vargas, J. M.; Denardin, J. C. Superparamagnetism and Other Magnetic Features in Granular Materials: A Review on Ideal and Real Systems. *J. Nanosci. Nanotechnol.* **2008**, *8*, 2836−2857.
(55) Cullity, B. D.; Graham, C. D. *Introduction to Magnetic Materials*; John Wiley & Sons, 2011.
(56) Xuan, S.; Wang, Y.-X. J.; Yu, J. C.; Cham-Fai Leung, K. Tuning the Grain Size and Particle Size of Superparamagnetic Fe_3O_4 Microparticles. *Chem. Mater.* **2009**, *21*, 5079−5087.
(57) Thong, P. Q.; Thu Huong, L. T.; Tu, N. D.; My Nhung, H. T.; Khanh, L.; Manh, D. H.; Nam, P. H.; Phuc, N. X.; Alonso, J.; Qiao, J.; Sridhar, S.; Thu, H. P.; Phan, M. H.; Kim Thanh, N. T. Multifunctional Nanocarriers of Fe_3O_4@PLA-PEG/Curcumin for MRI, Magnetic Hyperthermia and Drug Delivery. *Nanomedicine* **2022**, *17*, 1677−1693.
(58) Das, R.; Alonso, J.; Nemati Porshokouh, Z.; Kalappattil, V.; Torres, D.; Phan, M.-H.; Garaio, E.; García, J. A. ∴; Sanchez Llamazares, J. L.; Srikanth, H. Tunable High Aspect Ratio Iron Oxide Nanorods for Enhanced Hyperthermia. *J. Phys. Chem. C* **2016**, *120*, 10086−10093.
(59) Nemati, Z.; Alonso, J.; Martinez, L. M.; Khurshid, H.; Garaio, E.; Garcia, J. A.; Phan, M. H.; Srikanth, H. Enhanced Magnetic Hyperthermia in Iron Oxide Nano-Octopods: Size and Anisotropy Effects. *J. Phys. Chem. C* **2016**, *120*, 8370−8379.
(60) Attanayake, S. B.; Chanda, A.; Das, R.; Kapuruge, N.; Gutierrez, H. R.; Phan, M.-H.; Srikanth, H. Emergent Magnetism and Exchange Bias Effect in Iron Oxide Nanocubes with Tunable Phase and Size. *J. Phys.: Condens. Matter* **2022**, *34*, 495301.
(61) Noval, V. E.; Carriazo, J. G. Fe_3O_4-TiO_2 and Fe_3O_4-SiO_2 Core-Shell Powders Synthesized from Industrially Processed Magnetite (Fe_3O_4) Microparticles. *Mater. Res.* **2019**, *22*, No. e20180660.
(62) Kok, H.; Wust, P.; Stauffer, P.; Bardati, F.; van Rhoon, G.; Crezee, J. Current State of the Art of Regional Hyperthermia Treatment Planning: A Review. *Radiat. Oncol.* **2015**, *10*, 196.
(63) Lagendijk, J. J. W. Hyperthermia Treatment Planning. *Phys. Med. Biol.* **2000**, *45*, R61.
(64) Chou, C.-K. Use of Heating Rate and Specific Absorption Rate in the Hyperthermia Clinic. *Int. J. Hyperth.* **1990**, *6*, 367−370.
(65) Ring, H. L.; Sharma, A.; Ivkov, R.; Bischof, J. C. The Impact of Data Selection and Fitting on SAR Estimation for Magnetic Nanoparticle Heating. *Int. J. Hyperthermia* **2020**, *37*, 100−107.
(66) Andreu, I.; Natividad, E. Accuracy of Available Methods for Quantifying the Heat Power Generation of Nanoparticles for Magnetic Hyperthermia. *Int. J. Hyperthermia* **2013**, *29*, 739−751.
(67) Nemati, Z.; Alonso, J.; Rodrigo, I.; Das, R.; Garaio, E.; García, J. A. ∴; Orue, I.; Phan, M.-H.; Srikanth, H. Improving the Heating Efficiency of Iron Oxide Nanoparticles by Tuning Their Shape and Size. *J. Phys. Chem. C* **2018**, *122*, 2367−2381.
(68) Liu, Y.; Cui, T.; Li, Y.; Zhao, Y.; Ye, Y.; Wu, W.; Tong, G. Effects of Crystal Size and Sphere Diameter on Static Magnetic and Electromagnetic Properties of Monodisperse Fe_3O_4 Microspheres. *Mater. Chem. Phys.* **2016**, *173*, 152−160.
(69) Nguyen, M. D.; Deng, L.; Lee, J. M.; Resendez, K. M.; Fuller, M.; Hoijang, S.; Robles Hernandez, F. C.; Chu, C.-W.; Litvinov, D.; Hadjiev, V. G.; Xu, S.; Phan, M.-H.; Lee, T. R. Magnetic Tunability via Control of Crystallinity and Size in Polycrystalline Iron Oxide Nanoparticles. *Small* **2024**, *20*, 2402940.
(70) Rodrigo, I.; Castellanos-Rubio, I.; Garaio, E.; Arriortua, O. K.; Insausti, M.; Orue, I.; García, J. A. ∴; Plazaola, F. Exploring the Potential of the Dynamic Hysteresis Loops via High Field, High Frequency and Temperature Adjustable AC Magnetometer for Magnetic Hyperthermia Characterization. *Int. J. Hyperthermia* **2020**, *37*, 976−991.

https://doi.org/10.1021/acsami.4c22386
ACS Appl. Mater. Interfaces 2025, 17, 19436−19445